Supplementary Information

Superior energy storage performance of $PbZrO_3$-based films via phase regulation and entropy engineering

Jiaqi Lian[a], Fengzhen Huang[a,b*], Biwei Shen[a], Yulong Yang[a], Jielin Zha[a], Zeyu Xiao[a], Kai Cao[a], Xiaomei Lu[a,b*] and Jinsong Zhu[a,b]

[a] National Laboratory of Solid State Microstructures and Physics School, Nanjing University, Nanjing, 210093, P. R. China

[b] Collaborative Innovation Center of Advanced Microstructures, Nanjing University, Nanjing, 210093, P. R. China

Email: fzhuang@nju.edu.cn; xiaomeil@nju.edu.cn

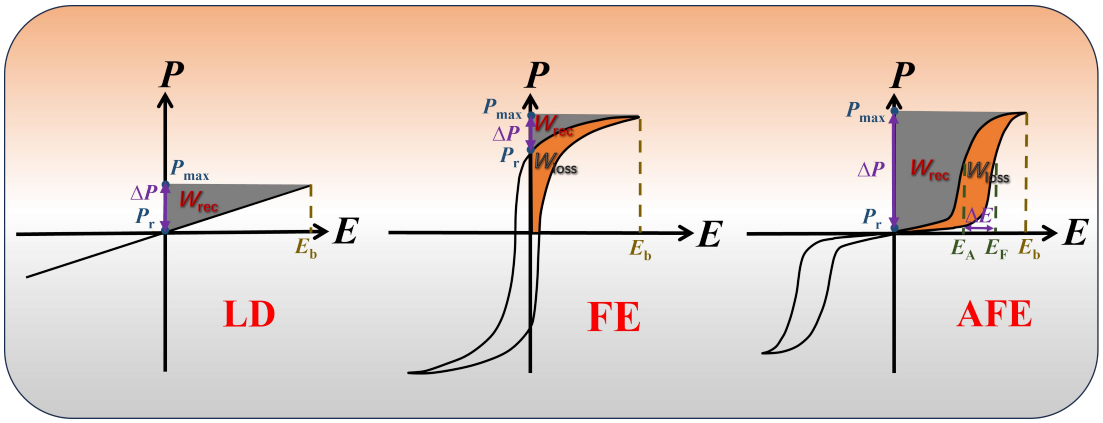

Fig. S1 *P-E* loops of linear dielectric (LD), ferroelectric (FE) and antiferroelectric (AFE).

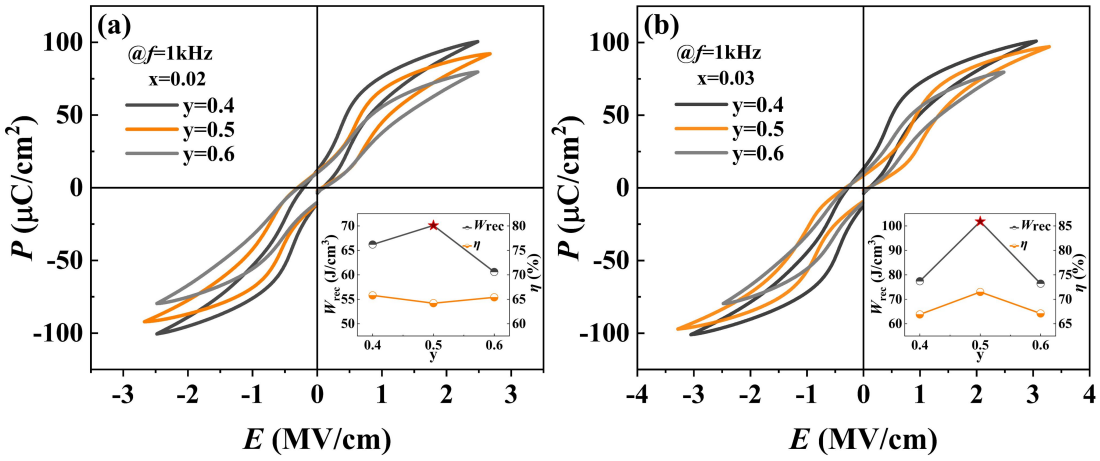

Fig. S2 *P-E* loops of (a) 0.02-PLSB/y-ZSO and (b) 0.03-PLSB/y-ZSO films measured near their respective E_b, with insets showing the dependence of W_{rec} and η on y.

Fig. S2 shows the *P-E* loops and their corresponding W_{rec} and η of x-PLSB/y-ZSO (x = 0.02, 0.03; y = 0.4, 0.5, 0.6) thin films. For different x, the films with a Zr/Sn ratio of 1:1 exhibit the highest W_{rec}.

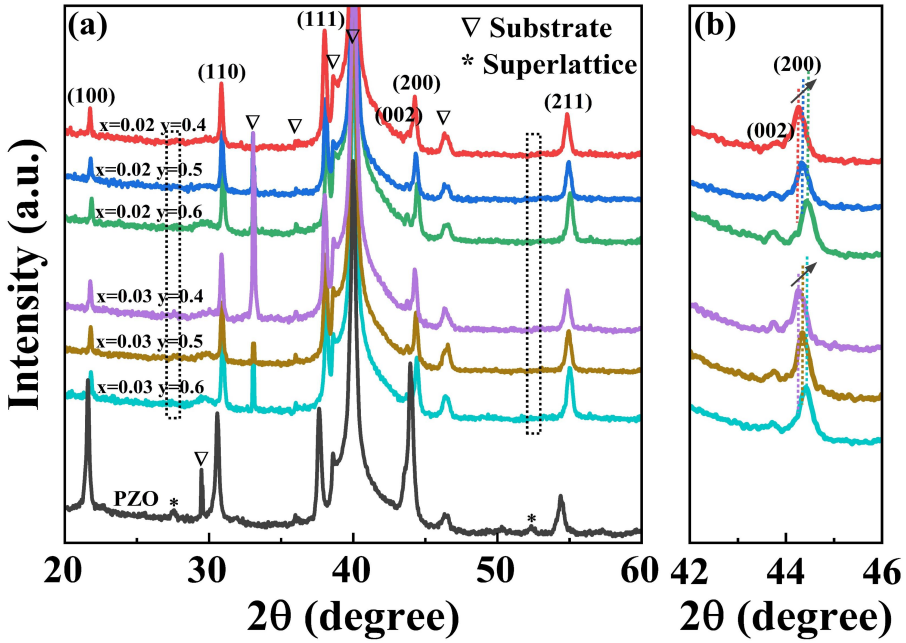

Fig. S3 (a) Room-temperature X-ray diffraction patterns of PZO, 0.02-PLSB/y-ZSO and 0.03-PLSB/y-ZSO films, and (b) a magnified view around the (200) diffraction peak.

Fig. S3(a) shows the room-temperature XRD patterns of PZO, 0.02-PLSB/y-ZSO and 0.03-PLSB/y-ZSO films, with all diffraction peaks indexed based on a pseudocubic structure. The results indicate that all the films exhibit a single-phase perovskite structure without detectable secondary phases. Fig. S3(b) shows a magnified view around the (200) diffraction peak. It is seen that the peak gradually shifts toward higher angles with increasing y, indicating the substitution of larger-radius Zr^{4+} (0.72 Å) by smaller-radius Sn^{4+} (0.69 Å). Notably, the intensity of (002) corresponding to the AFE_T increases with increasing y, implying that Sn^{4+} ions induce the appearance of AFE_T and thus the coexistence of AFE_O and AFE_T in x-PLSB/y-ZSO films. In addition, as the increase of x or y, the superlattice diffraction peaks (marked with *) gradually weaken and then become indistinguishable, indicating the disruption of long-range AFE order.

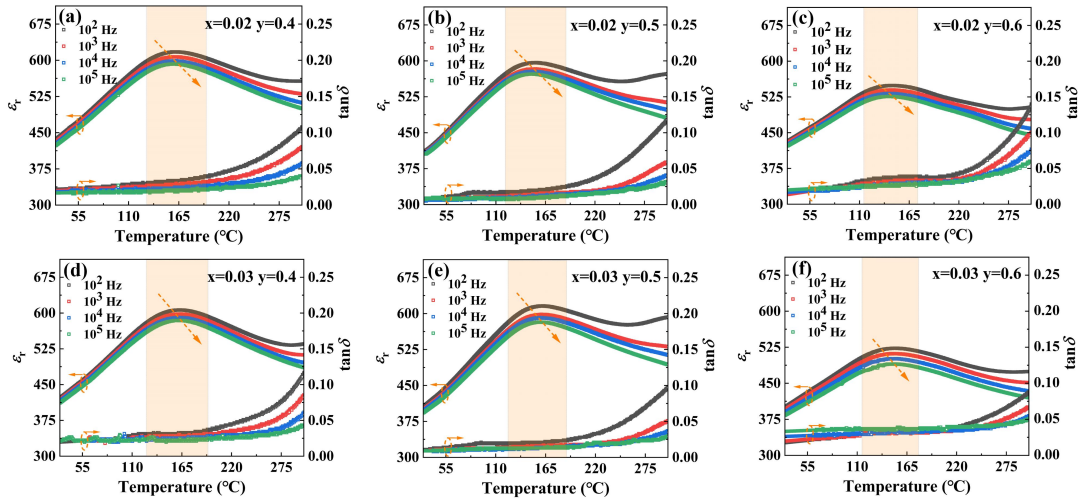

Fig. S4 Temperature-dependent dielectric constant (ε_r) and loss (tanδ) of 0.02-PLSB/y-ZSO and 0.03-PLSB/y-ZSO films.

Fig. S4(a)-(f) show the temperature-dependent dielectric constant (ε_r) and loss (tanδ) of 0.02-PLSB/y-ZSO and 0.03-PLSB/y-ZSO films over the temperature range of 30-300 ℃. The results indicate that the dielectric-constant peak gradually shifts toward room temperature and broadens with increasing y. It means that, on the one hand, the phase transition temperature from AFE to paraelectric shifts toward room temperature since $PbSnO_3$ possesses a lower phase-transition temperature than that of PZO.[53] On the other hand, the introduction of Sn^{4+} ions and their random distribution at the B site enhance the relaxor degree of the phase transition, leading to peak broadening. Furthermore, the competition of AFE_O and AFE_T can hinder the growth of grain and domain sizes, resulting in lower tanδ for the films with Zr/Sn ratio equaling 1:1, contributing to their strongest E_b and highest W_{rec}.

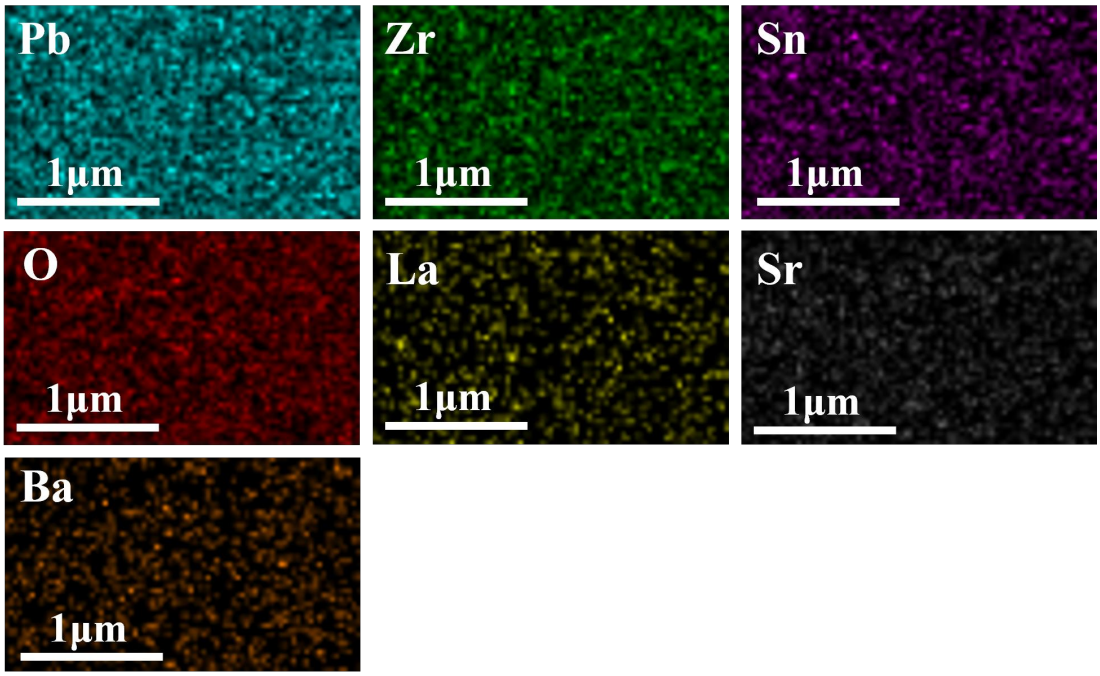

Fig. S5 EDS mapping of the surface elemental distribution of the 0.03-PLSB/0.5-ZSO thin film.

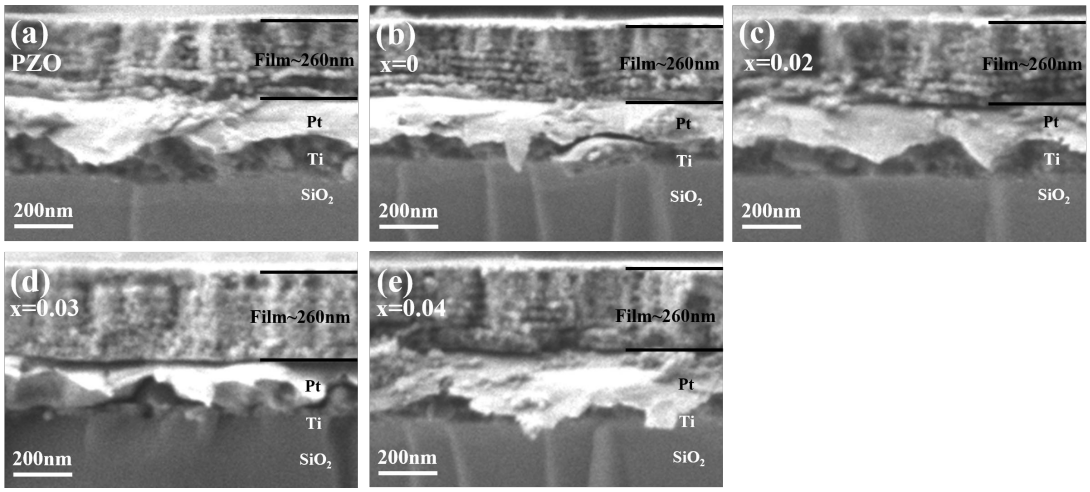

Fig. S6 Cross-sectional SEM images of PZO and x-PLSB/0.5-ZSO thin films.

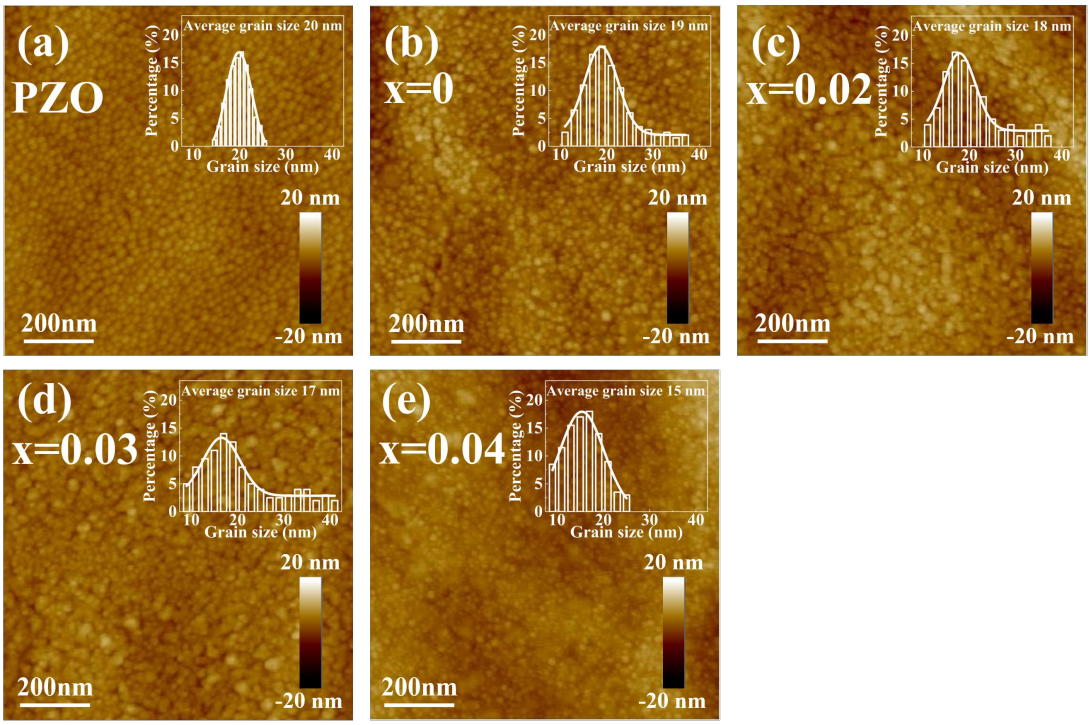

Fig. S7 AFM surface morphologies of PZO and x-PLSB/0.5-ZSO thin films, with insets showing grain size distributions.

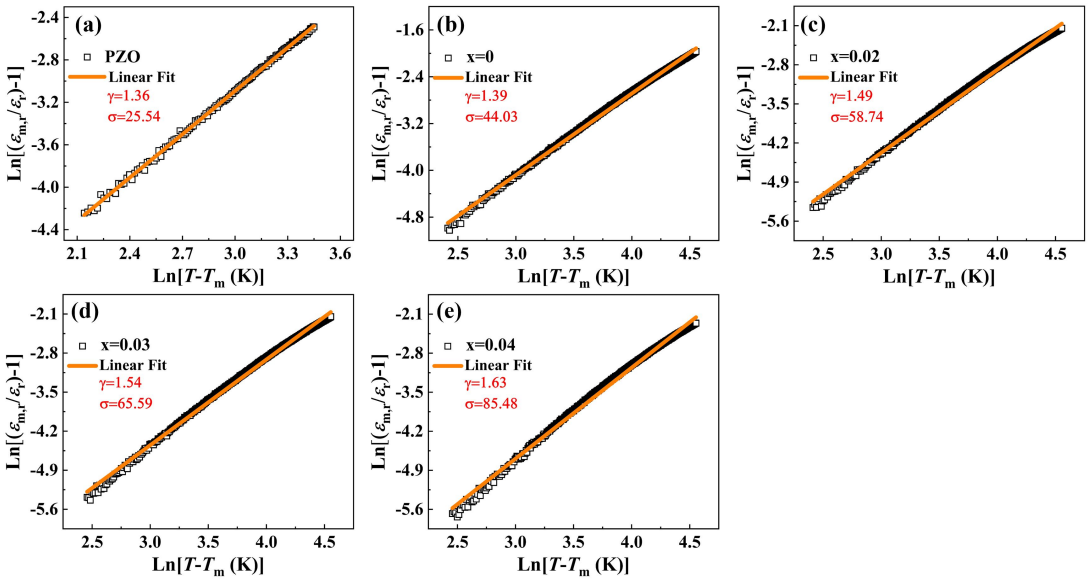

Fig. S8 Plots of $ln\left[(\varepsilon_{m,r}/\varepsilon_r)-1\right]$ versus $ln(T-T_m)$ at 1 kHz for PZO and x-PLSB/0.5-ZSO thin films, extracted from their temperature-dependent dielectric properties.

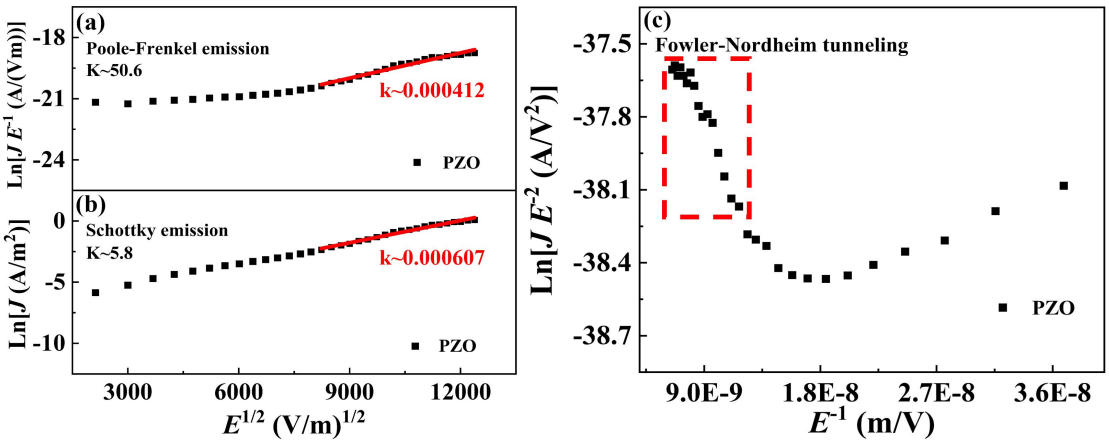

Fig. S9 Fitting results for PZO film based on (a) Poole-Frenkel emission, (b) Schottky emission and (c) Fowler-Nordheim tunneling mechanisms.

In dielectric materials, conduction mechanisms are generally categorized into bulk-limited processes (e.g., Ohmic conduction, space-charge-limited conduction (SCLC), and Poole-Frenkel (P-F) emission) and interface-limited processes (e.g., Schottky emission and Fowler-Nordheim (F-N) tunneling). The former are determined by carrier concentration, mobility and charge-defect-related trap energy levels, whereas the latter are governed by carrier injection across interfacial barriers.

The five conduction mechanisms satisfy the following mathematical expressions:[54]

Ohmic: $J = \sigma E$ (S1)

SCLC: $J = \frac{9\mu\varepsilon_0\varepsilon_r}{8d}E^2$ (S2)

P-F emission: $J = e\mu N_c E \cdot exp\left[\frac{-e(\phi_{PF}-\sqrt{eE/\pi\varepsilon_0 K})}{k_B T}\right]$ (S3)

Schottky emission: $J = AT^2 \cdot exp\left[\frac{-e(\phi_S-\sqrt{eE/4\pi\varepsilon_0 K})}{k_B T}\right]$ (S4)

F-N tunnelling: $J = \frac{e^2E^2}{8\pi h\phi_S} \cdot exp\left[-\frac{8\pi\sqrt{2em_T^*{\phi_S}^3}}{3hE}\right]$ (S5)

where σ, μ, ε_0, ε_r, d, e, k_B, T, N_c, ϕ_{PF}, K, A, ϕ_S, h, m_T^* are electrical conductivity, electron mobility, vacuum dielectric constant, relative dielectric constant, film thickness, electron charge, Boltzmann constant, absolute temperature, density of states in the conduction band, P-F

emission barrier, optical dielectric constant, Richardson constant, Schottky barrier height, Planck constant, and electron tunneling effective mass, respectively. The mathematical expressions describing P-F conduction ($ln\frac{J}{E}=\frac{\sqrt{e/\pi\varepsilon_0 K}}{k_B T}E^{1/2}-\frac{e\phi_{PF}}{k_B T}+lne\mu N_c$), Schottky emission ($lnJ=\frac{\sqrt{e/4\pi\varepsilon_0 K}}{k_B T}E^{1/2}-\frac{e\phi_S}{k_B T}+lnAT^2$) and F-N tunneling ($ln\frac{J}{E^2}=-\frac{8\pi\sqrt{2em_T^*{\phi_S}^3}}{3h}E^{-1}+ln\frac{e^2}{8\pi h\phi_S}$) can be linearized. As shown in Fig. S9(a) and (b), $E^{1/2}$ is adopted as the x-axis, while $\ln\frac{J}{E}$ and $\ln J$ are plotted as the y-axis for the P-F conduction and Schottky emission, respectively. Linear fitting of the high-field regions (red lines) yield slopes corresponding to optical dielectric constants *K* of 50.6 and 5.8. For PZO, the optical dielectric constant *K* is generally reported to lie in the range of 4.84 to 7.84.[55] Accordingly, the extracted *K* value from Schottky emission is reasonable, while that obtained from the P-F emission exceeds the reasonable range. Moreover, as shown in Fig. S9(c), the F-N tunneling fitting exhibits poor linearity in the high-field region (highlighted by the red dashed box), excluding this mechanism as well. Taken together, these results indicate that the high-field conduction in PZO film is primarily governed by the Schottky emission. Compared with x-PLSB/0.5-ZSO films, more V_{Pb}^{2-} and V_O^{2+} are involved in PZO, which increase the charge-defect-related trap states at the film/electrode interface, lower the interface barrier height, and therefore facilitate the carrier injection.

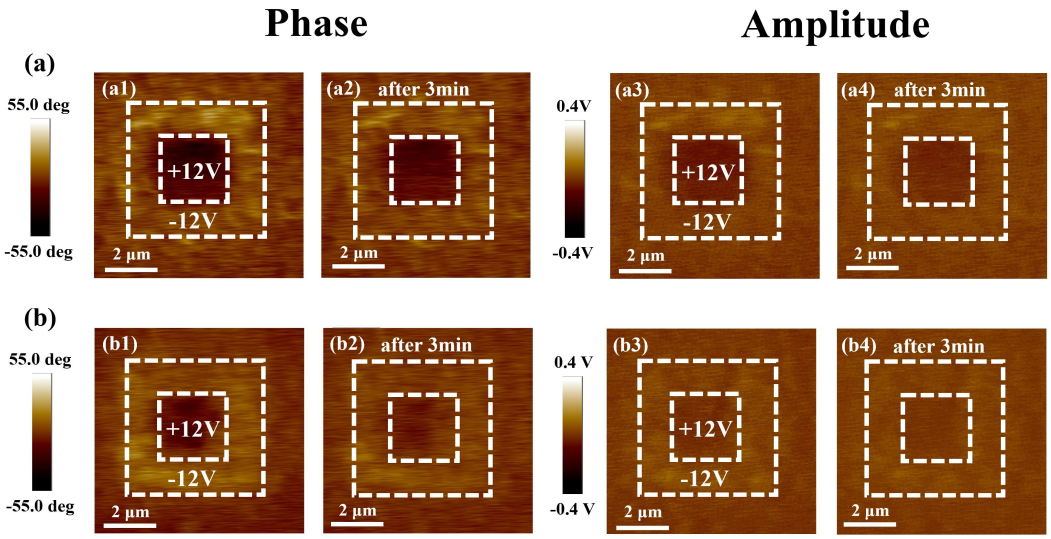

Fig. S10 Time evolution of out-of-plane PFM images of (a) PZO and (b) x-PLSB/0.5-ZSO films after poling with -12 V in 5×5 μm^2 and then with +12 V in 2×2 μm^2 regions.

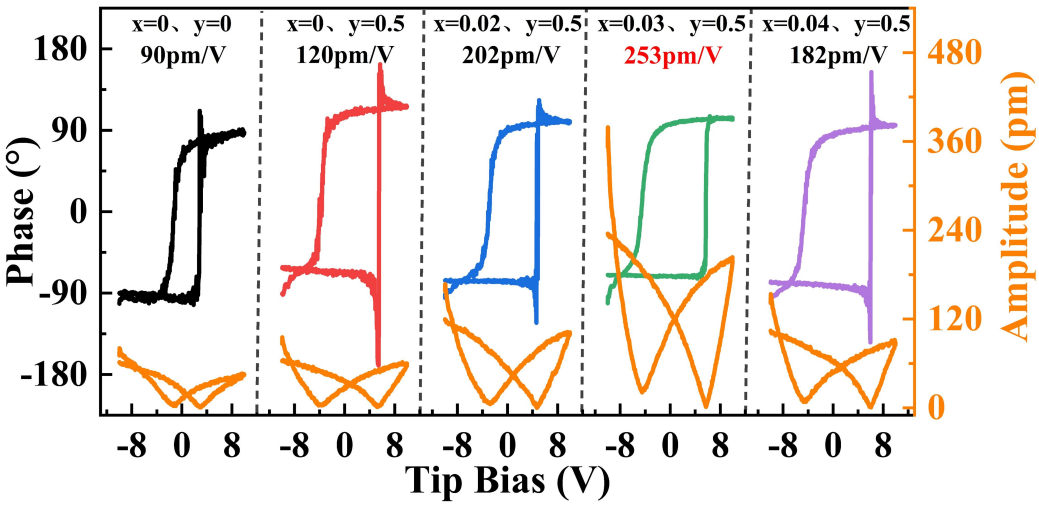

Fig. S11 Piezoelectric phase and amplitude of PZO and x-PLSB/0.5-ZSO films.

Effective piezoelectric coefficient is determined by piezoresponse force microscopy (PFM). During the measurement, an AC voltage is applied to drive the local piezoelectric response, while a DC bias is swept to switch the polarization. Based on the above amplitude-voltage loops, the effective piezoelectric coefficient corresponds to the ratio of the maximum amplitude to the applied AC voltage (0.8 V), and the largest value (~253 pm V^{-1}) is obtained in the 0.03-PLSB/0.5-ZSO film.

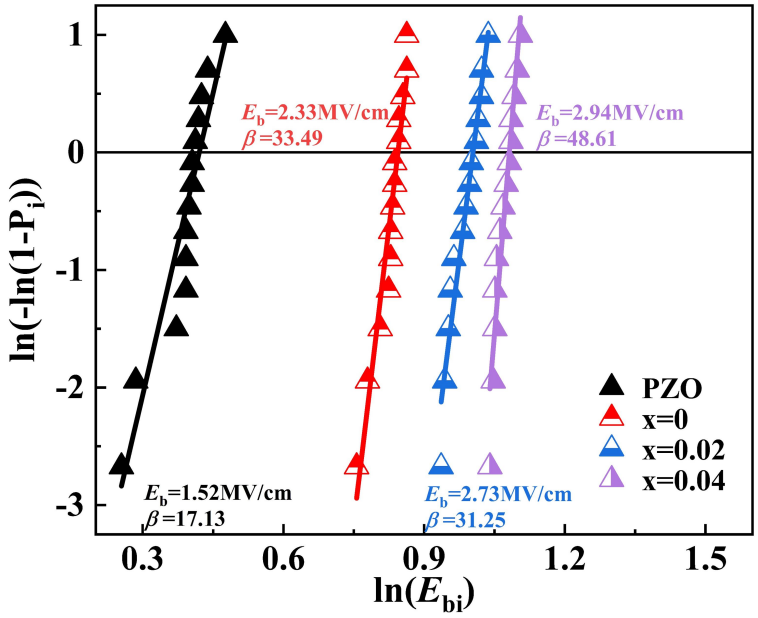

Fig. S12 Weibull distribution of E_b for PZO and x-PLSB/0.5-ZSO films.